


Erratum: Optical response and band structure of LiCoO₂ including electron-hole interaction effects [Phys. Rev. B **104**, 115120 (2021)]

Santosh Kumar Radha, Walter R. L. Lambrecht , Brian Cunningham, Myrta Grüning, Dimitar Pashov, and Mark van Schilfgaarde



(Received 28 August 2023; published 30 October 2023)

The calculation of optical properties of LiCoO₂ presented in Phys. Rev. B **104**, 115120 (2021) are revisited with improved accuracy calculations. An error in the polarization dependence in the previous work is pointed out and corrected here. The exciton binding energies are found to be somewhat smaller than previously reported—about 0.9 eV rather than 2 eV. The spatial extent of the excitons is analyzed here and shows interesting differences between dark and bright excitons. The effects of the local field effects are also clarified and found to be largest in the direction perpendicular to the layers.

DOI: [10.1103/PhysRevB.108.159902](https://doi.org/10.1103/PhysRevB.108.159902)

In the original paper, it was shown that the lowest absorption peaks in the visible-UV region are excitonic in nature and the exciton binding energies were found to be exceptionally high—about 2 eV for the lowest excitons. Since the publication of that paper, improvements have been made to the QUESTAAL codes [1,2] used in this work, which allow for more stringent convergence tests and new analysis tools. In the course of further studying the real space localization of the excitons, differences were found in the optical dielectric function from the original work, which led us to identify an error in the original work with respect to the polarization dependence of the dielectric function. The purpose of this Erratum is to correct this error and to provide further analysis of the spatial localization of the excitons.

In the original paper the Cartesian coordinate system (which we will here denote with primes) was chosen so that one of the rhombohedral lattice vectors was along x' , the y' axis was in the plane of the first two rhombohedral vectors, and the z' axis perpendicular to it. The primitive lattice vectors were then $\mathbf{a}_1 = a\hat{x}'$, $\mathbf{a}_2 = a \cos \gamma \hat{x}' + a \sin \gamma \hat{y}'$, $\mathbf{a}_3 = \cos \gamma \hat{x}' + a \sin \gamma \sin \beta \hat{y}' + a \sin \gamma \cos \beta \hat{z}'$ with a the rhombohedral lattice constant, γ the angle between any two rhombohedral vectors, and $\sin \beta = \cos \gamma (1 - \cos \gamma) / \sin^2 \gamma$ so that $\mathbf{a}_1 \cdot \mathbf{a}_2 = \mathbf{a}_1 \cdot \mathbf{a}_3 = \mathbf{a}_2 \cdot \mathbf{a}_3 = a^2 \cos \gamma$.

The choice of Cartesian coordinates does not affect the band structure but does affect the form of the dielectric tensor. The latter is diagonal only when the Cartesian axes are chosen as the principal axes which should coincide with the symmetry axes of the system. When the z axis is chosen as the threefold symmetry axis, it corresponds to the direction of $\mathbf{a}_1 + \mathbf{a}_2 + \mathbf{a}_3$. Choosing the x axis along the projection of one of the rhombohedral lattice vectors on the plane perpendicular to the z axis, we obtain a symmetry adapted choice of Cartesian coordinates with the xz plane a mirror plane and y a twofold symmetry axis of the point group D_{3d} . In that case, threefold symmetry will guarantee that $\epsilon_{xx} = \epsilon_{yy} \neq \epsilon_{zz}$. The z axis then also corresponds to the \mathbf{c} axis of the hexagonal conventional supercell corresponding to the rhombohedral lattice, which consists of an ABC stacking of the hexagonal layers. In the original paper, the dielectric function was calculated along \hat{z}' and along $(\hat{x}' + \hat{y}')/\sqrt{2}$ and these were labeled erroneously as, respectively, $\parallel \mathbf{c}$ and $\perp \mathbf{c}$. In fact, the old z' direction is closer to the direction $\perp \mathbf{c}$. The result is that the dielectric functions were not corresponding to the principal axes of the tensor and had hence incorrect oscillator strength. Besides this mistake, some convergence issues and numerical parameter settings affected the results of the original paper, which were obtained with an early version of the codes. Rather than correcting each figure, we here provide new results with improved calculations and furthermore add new information on the localization of the excitons.

The correct dielectric functions along the principal axes are shown in Fig. 1 in the independent particle approximation (IPA) and Bethe-Salpeter equation (BSE) approximation. We can see that the intensity of the main peaks is significantly higher perpendicular to the threefold symmetry axis \mathbf{c} in BSE. The BSE ϵ_2 is rather strongly suppressed for $\mathbf{E} \parallel \mathbf{c}$. This turns out to be mainly a result of the local field corrections and occurs already in the random phase approximation (RPA), as shown in Fig. 2. It is typical of layered materials in the direction perpendicular to the layers. We here calculated the RPA and IPA dielectric function directly at a \mathbf{q} point close to $\mathbf{q} = 0$ but approaching $\mathbf{q} \rightarrow 0$ from different directions. The value at $\mathbf{q} = 0$ on the other hand is obtained with analytically calculated velocity matrix elements and is seen to somewhat overestimate the matrix elements, which is related to the approximate calculation of the $d\Sigma/dk$ contribution from the nonlocal self-energy.

The BSE still shows large excitonic effects but the shape of the spectrum is nonetheless significantly different from that in the original paper and the exciton binding energy of the lowest bright exciton is about 0.9 eV rather than about 2 eV. The lowest bright exciton occurs near 2 eV rather than 1.5 eV. The shape of the BSE spectrum for $\mathbf{E} \perp \mathbf{c}$ is close to the $\mathbf{E} \parallel \hat{z}'$ in the original paper but is overall shifted toward higher energy, in spite of the fact that the latter had a larger quasiparticle gap.

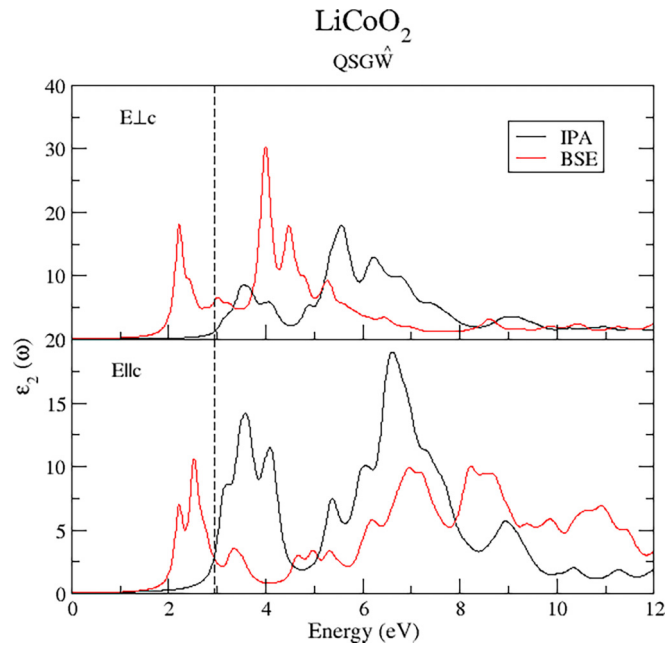


FIG. 1. Imaginary part of the dielectric function along principal axes and in the independent particle approximation (IPA) and the Bethe-Salpeter equation (BSE) approximation.

The quasiparticle gap in the QSGW approach is also significantly lower than in the original work. This results from different convergence; while nine valence bands and five conduction bands were included in the two-particle Hamiltonian active space in the present calculation, only four valence bands were included in the original paper. The choice used now includes the six O-2*p* bands and the three Co-*t*_{2*g*} bands as occupied bands and the two Co-*e*_g and several higher conduction bands which were shown in previous work to include the Li-*sp* derived bands [3]. We have further verified that adding O-2*s* bands changes the gap by less than 0.05 eV. The inclusion of more bands in the active space leads to a stronger reduction of *W* due to the electron-hole effects. The smallest indirect QSGW gap is found to be 2.95 eV and the direct gap at Γ is 4.00 eV, which compare with 3.762 and 4.884 eV in Table I of the original paper. The self-energy Σ was converged to better than 5×10^{-4} root-mean-square deviation between successive iterations and provides gaps converged to within 0.03 eV both in terms of the self-consistency and the number of bands included. The QSGW gaps without *W* calculated in the random phase approximation, i.e., not including ladder diagrams, remained within the error bar close to those in the original paper. The results labeled as GGA (generalized gradient approximation) were actually obtained in the local density approximation (LDA) using the von Barth–Hedin exchange-correlation potential (also used here), but in terms of the gaps this makes little difference. Both the QSGW results and the QSGW results are independent of this starting approximation.

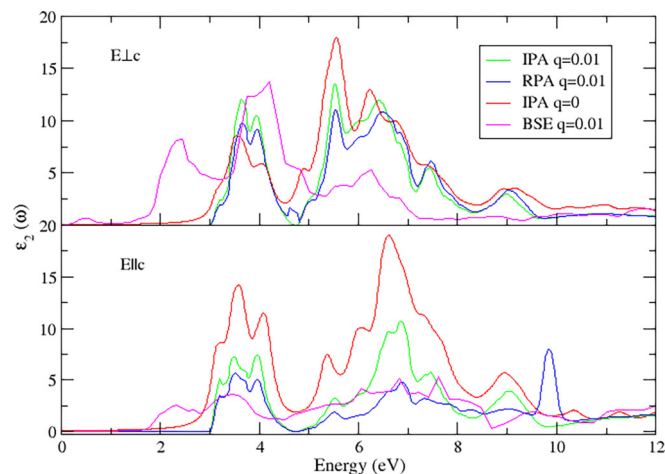


FIG. 2. Comparison of independent particle approximation (IPA) with the random phase approximation (RPA) imaginary part of the dielectric function. The latter includes local field corrections while the former does not.

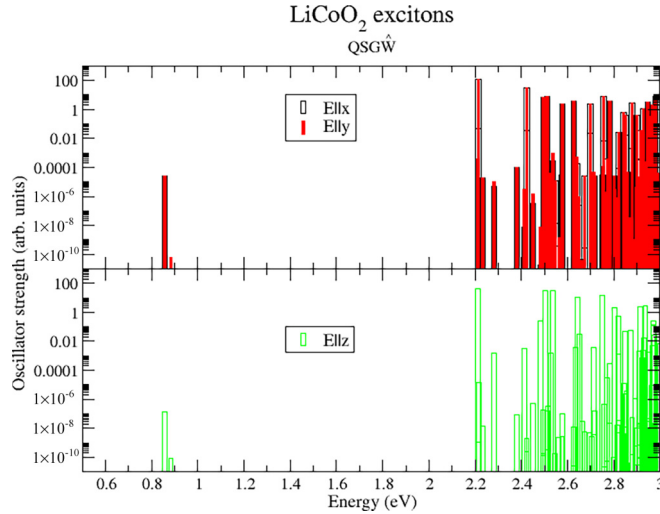


FIG. 3. Two-particle Hamiltonian eigenvalues with oscillator strength contributing to $\epsilon_2(\omega)$.

To further inspect the excitons, Fig. 3 shows a bar graph of the individual eigenvalues of the two-particle Hamiltonian, with their oscillator strength in x , y , and z directions on a logarithmic scale. One can see that the x and y oscillator strengths are exactly the same and dark excitons are identified at 0.86 (doubly degenerate) and 0.88 eV (nondegenerate) below the first bright excitons at 2.211 (nondegenerate) and 2.215 eV (doubly degenerate). Several more dark and bright excitons are seen but they appear concentrated in the region between 2.0 and the quasiparticle gap at ~ 3.0 eV. No excitons occur near 1.5 eV. Interestingly, when calculating the BSE dielectric function at finite \mathbf{q} , shown in Fig. 2, we can see a weak peak for $\mathbf{E} \perp \mathbf{c}$ below 1 eV close to but even lower than the dark exciton calculated at $\mathbf{q} = 0$. It thus appears that this dark exciton may become slightly allowed at finite \mathbf{q} with a matrix element proportional to q and also that this exciton disperses downward in energy with q .

In comparing to the various experimental data, it appears that our lowest optical exciton being near 2.0 eV is consistent with the data of Refs. [4,5] who report onsets ~ 2 eV from Tauc plots and Kushida and Kuriyama [6] who report a main absorption band at 2 eV related to d - d transitions but less well with [7] who found lower energy absorption features near 1.7 eV in differential absorption, identified as the gap in their paper, and lower energy features at ~ 0.8 and ~ 0.65 eV. Liu *et al.* [8] also found an absorption feature around 1.7 eV but mostly for Li_xCoO_2 with $x < 1$. The experimental situation is thus still confusing, in large part because of different types of micro- or nanostructure and different Li content in the samples resulting from different synthesis conditions.

Finally, we add some new information on the localization of the excitons. The \mathbf{k} space and band contributions to a few of the excitons are given in Fig. 4. In this figure for each valence band v at \mathbf{k} and a given exciton λ , the $W_{v\mathbf{k}}^\lambda = \sum_c |A_{v\mathbf{k}c}^\lambda|^2$ is indicated as a colored circle of size proportional to $W_{v\mathbf{k}}^\lambda$ and likewise for the conduction bands $W_{c\mathbf{k}}^\lambda = \sum_v |A_{v\mathbf{k}c}^\lambda|^2$, with $A_{v\mathbf{k}c}^\lambda$ the eigenvector of exciton λ in the transition state basis. The values are interpolated to the symmetry lines from the computed grid of \mathbf{k} values used in the two-particle Hamiltonian. We can see that consistent with the original paper, the excitons are very broadly spread in \mathbf{k} space and mainly arising from the top three and bottom two conduction bands, which are $\text{Co-}d_{t2g}$ and $\text{Co-}d_{eg}$ type bands, respectively. Nonetheless, we can now see some difference between the dark and the bright excitons. The dark excitons are more uniformly spread throughout the entire Brillouin zone, while the bright excitons are a bit more localized near the maxima and minima along Γ - M and Γ - K and along L - A and A - H . We here use the $k_z = 0$ (M - Γ - K) and $k_z = 3\pi/c$ (L - A - H) slices of the hexagonal conventional cell Brillouin even though we still use a primitive rhombohedral cell. Here, c is the lattice constant of the hexagonal cell along the main symmetry axis z . The L - A - H plane lies in the top plane of the rhombohedral zone. We can also see that the top valence band makes a stronger contribution for the bright exciton polarized along \mathbf{c} .

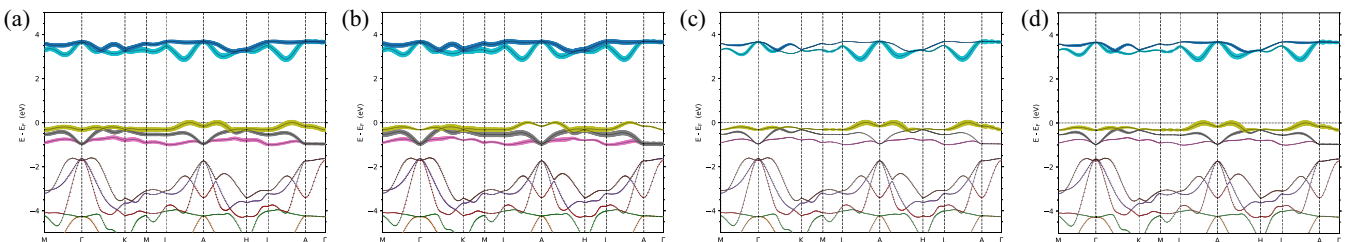


FIG. 4. Band weights of the excitons: (a) lowest dark, (b) second dark, (c) lowest bright in $\mathbf{E} \parallel \mathbf{c}$, and (d) lowest bright in $\mathbf{E} \perp \mathbf{c}$, in order of increasing energy.

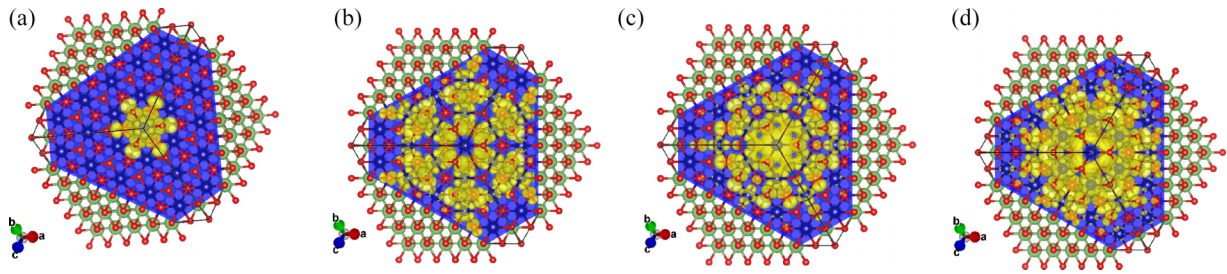


FIG. 5. Exciton wave functions for (a) lowest dark, (b) second dark, (c) lowest bright exciton in $\mathbf{E} \parallel \mathbf{c}$, and (d) lowest bright in $\mathbf{E} \perp \mathbf{c}$ polarizations. The yellow isosurface shows $|\Psi(\mathbf{r}_h, \mathbf{r}_e)|^2$ for fixed \mathbf{r}_h hole position as a function of the \mathbf{r}_e electron position. The blue plane presents a cut through a (111) plane of the structure just below the central Co where the hole is located and the atoms above it were removed from the figure except for the first layer of O atoms. Co, blue; Li, green; O, red spheres. The isosurface level is taken at 2% of the maximum value.

The real space extent of a few excitons is illustrated in Fig. 5. We can see that the first dark exciton is highly localized on the central Co and its six nearest neighbor O atoms, while the second is significantly more delocalized. The bright exciton in the $\mathbf{E} \perp \mathbf{c}$ polarization, on the other hand, shows no contribution on the central Co but rather on its six nearest neighbor Co and the O linking them to the central O. The z -polarized exciton shows contributions on the central Co and extending out to two rings of Co neighbors. They are similar in delocalization to the second dark exciton. Similarly, Fig. 6 shows how the holes are distributed when the electron is fixed at the central Co. In all cases, we can see that the exciton is strongly confined close to the Co plane on which either hole or electron is fixed. We can see that although all the excitons come primarily from the Co- d bands, the electron and hole localizations are different.

In summary, a mistake in labeling the polarization dependence of the optical dielectric function that occurred in the original paper because of an inopportune choice of Cartesian axes was here corrected. Improved calculations confirm the existence of strongly bound excitons in LiCoO₂ but with slightly lower binding energies. The spatial localization of the low-lying excitons was calculated and shows localization within the first few neighbors with considerable charge-transfer characteristics rather than a Frenkel exciton localized on a single Co atom.

W.L. was supported by the Air Force Office of Scientific Research under Grant No. FA9550-22-1-0201. The calculations made use of the High Performance Computing Resource in the Core Facility for Advanced Research Computing at Case Western Reserve University. M.v.S. and D.P. were supported by the Computational Chemical Sciences program within the Office of Basic Energy Sciences, U.S. Department of Energy under Contract No. DE-AC36-08GO28308, at the National Renewable Energy Laboratory, operated by Alliance for Sustainable Energy, LLC. We also acknowledge the use of the Eagle facility at NREL, sponsored by the Office of Energy Efficiency and also the National Energy Research Scientific Computing Center, under Contract No. DE-AC02-05CH11231 using NERSC award BES-ERCAP0021783.

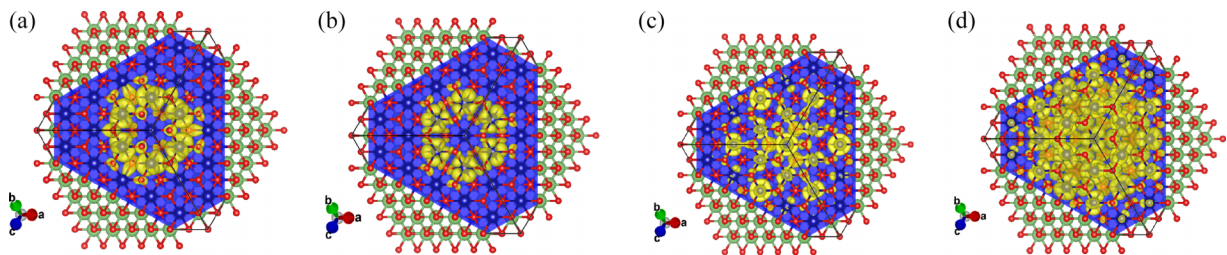


FIG. 6. Exciton wave functions for (a) lowest dark, (b) second dark, (c) lowest bright exciton in $\mathbf{E} \parallel \mathbf{c}$, and (d) lowest bright in $\mathbf{E} \perp \mathbf{c}$ polarizations. The yellow isosurface shows $|\Psi(\mathbf{r}_h, \mathbf{r}_e)|^2$ for fixed \mathbf{r}_e electron position as a function of the \mathbf{r}_h hole position. The blue plane presents a cut through a (111) plane of the structure passing through the central Co where the hole is located and the atoms above it were removed from the figure except for the first layer of O atoms. Co, blue; Li, green; O, red spheres. The isosurface level is taken at 2% of the maximum value.

- [1] B. Cunningham, M. Grüning, D. Pashov, and M. van Schilfgaarde, $QSG\widehat{W}$: Quasiparticle self-consistent GW with ladder diagrams in W , [Phys. Rev. B **108**, 165104 \(2023\)](#).
- [2] D. Pashov, S. Acharya, W. R. Lambrecht, J. Jackson, K. D. Belashchenko, A. Chantis, F. Jamet, and M. van Schilfgaarde, Questaal: A package of electronic structure methods based on the linear muffin-tin orbital technique, [Comput. Phys. Commun. **249**, 107065 \(2019\)](#).
- [3] S. K. Radha and W. R. L. Lambrecht, Spin-polarized two-dimensional electron/hole gases on LiCoO_2 layers, [SciPost Phys. **10**, 057 \(2021\)](#).
- [4] T. Balakrishnan, N. Sankarasubramanian, A. Kavitha, and A. Kathalingam, Studies on structural, optical, electrical and morphological properties of LiCoO_2 thin films prepared by sol-gel method, [Mater. Res. Innovations **23**, 216 \(2019\)](#).
- [5] M. C. Rao, Optical absorption studies of LiCoO_2 thin films grown by pulsed laser deposition, [Int. J. Pure Appl. Phys. **6**, 365 \(2010\)](#).
- [6] K. Kushida and K. Kuriyama, Optical absorption related to Co-3d bands in sol-gel grown LiCoO_2 films, [Solid State Commun. **118**, 615 \(2001\)](#).
- [7] P. Ghosh, S. Mahanty, M. Raja, R. Basu, and H. Maiti, Structure and optical absorption of combustion-synthesized nanocrystalline LiCoO_2 , [J. Mater. Res. **22**, 1162 \(2007\)](#).
- [8] H. L. Liu, T. Y. Ou-Yang, H. H. Tsai, P. A. Lin, H. T. Jeng, G. J. Shu, and F. C. Chou, Electronic structure and lattice dynamics of Li_xCoO_2 single crystals, [New J. Phys. **17**, 103004 \(2015\)](#).